Focused Synthetic Aperture Radar Processing of Ice-Sounder Data Collected Over the Greenland Ice Sheet

Justin J. Legarsky, *Member, IEEE*, Sivaprasad P. Gogineni, *Fellow, IEEE*, and Torry L. Akins

Abstract—We developed a synthetic aperture radar (SAR) processing algorithm for airborne/spaceborne ice-sounding radar systems and applied it to data collected in Greenland. By using focused SAR (phase-corrected coherent averaging), we improved along-track resolution by a factor of four and provided a 6-dB processing gain over unfocused SAR (coherent averaging without phase correction) based on a point-target analysis for a Greenland ice-sounding data set. Also, we demonstrated that the focused-SAR processing reduced clutter and enabled us to identify bedrock-interface returns buried in clutter. Using focused-SAR technique, we processed data collected over a key 360-km-long portion of the 2000-m contour line of southwest Greenland. To the best of our knowledge, these are the first high-quality radar ice thickness measurements over this key location. Moreover, these ice-thickness measurements have been used for improving mass-balance estimates of the Greenland ice sheet.

Index Terms—Airborne radar, Greenland, ice, ice thickness, remote sensing, sounding, synthetic aperture radar (SAR).

I. INTRODUCTION

THE MASS balance of the polar ice sheets is a key variable in assessing the effect of ice sheets on sea level rise. There are two approaches for determining the mass balance of an ice sheet: 1) volumetric method and 2) flux method. Using the volumetric method, the periodic measurements of an ice-sheet elevation are made and compared to determine the elevation change. ICESat, a NASA satellite, tentatively scheduled to be launched in 2002, will use a precision laser altimeter to measure the ice-sheet elevation over its lifetime for monitoring changes in the mass balance using the volumetric method. Using the flux method, the mass balance is computed using net accumulation and total output flux, which requires ice-thickness measurements. Also, ice thickness is a key variable in the study of ice dynamics.

We developed a coherent radar depth sounder operating at 150 MHz and used it to collect a large volume of ice-sounding radar data on the Greenland ice sheet over the last few years. We employed both normal coherent and incoherent integration techniques to improve the SNR for obtaining good estimates of the ice thickness over much of the ice sheet. However, improved radar performance beyond that obtainable with integration is required to obtain ice-thickness measurements in a few areas; for example, the main channel of Jakobshavn outlet and some valleys in the southwest area of Greenland [1]. There are three main ways of obtaining this improved performance: 1) increased transmitter power; 2) increased receiver sensitivity; and 3) additional signal processing gain through coherent processing. We chose the third option: further processing with a focused-SAR algorithm because of the clutter reduction, which is not obtainable from the first two choices. The improved along-track resolution is obtained by focusing, which is a SAR-processing approach applied here to glacial ice.

Similar SAR techniques have been applied to ground penetrating radar (GPR) systems [2], [3]. The GPR systems typically operate near the surface. However, the Apollo lunar sounder radar system used SAR techniques from space for ground penetration [4].

The airborne ice-sounding radar (ISR) focused-SAR concept is based on well-known SAR techniques [5], [6]. Moreover, incoherent processing (averaging of power) and unfocused-SAR processing (coherent averaging without phase correction) techniques for ice-sounding data are well documented [7]–[11]. Raju and Moore [12] presented an incoherent form of the algorithm that involves cross correlating a number of reference functions with ISR data. Here we introduce phase corrections for the focused-SAR processing of airborne ISR that take into account a sloped ice surface.

II. GREENLAND DATA COLLECTION

A. Airborne Platform

A NASA P-3 aircraft provides an airborne platform for the ice-sounding radar system during Greenland data collection. The aircraft missions are normally flown out of either Thule Air Force Base or the Kangerlussuaq Airport in Greenland. The aircraft normally flies at an altitude of 500 m above the ice surface with an airspeed of about 130 m/s^{-1} during the Greenland missions. Also, the aircraft is equipped with a navigation system controlled by the global positioning system (GPS) and a scanning laser ranging instrument for measuring surface topography.

We have used this airborne system to collect a large volume of data since 1993, obtaining clear echoes from the bottom as well as from layers near the bedrock over the new European deep drill site [13], many outlet glaciers [14], and a hill (we detected it under the ice sheet) in north-central Greenland [15].

TABLE I
SUMMARY OF THE RADAR PARAMETERS FOR THE UNIVERSITY OF KANSAS
ICE-SOUNDING RADAR USED TO COLLECT DATA OVER THE GREENLAND ICE
SHEET FOR THIS STUDY

Description	Characteristic	Units
Radar Type	Pulse Compression	---
RF Carrier Frequency	150	MHz
Transmitted Pulse Width	1.6	μs
Compressed Pulse Width	60	ns
Peak Transmit Power	~100	W
A/D Dynamic Range	12 (72)	bit (dB)
Sampling Period	53.3 (18.75)	ns (MHz)

In Greenland, ice thickness measurements extracted from the radar data are playing an important role in current mass-balance studies [16], [17].

B. Radar Data

We collected ice-sounding data throughout Greenland using the University of Kansas ice-sounding radar system [18]. The ice sounder is a pulse compression radar system [19]. The coherent system is synchronized to a master clock operating at frequency of 37.5 MHz. A summary of the radar parameters is given in Table I. The modern system has sounded the deep ice $(\sim 3200 \text{ m})$ [13] from the summit of Greenland.

The coherent system records the in-phase (I) and quadrature (Q) components of the radar return signal. The I and Q components of the return signal are digitized by two 12-bit A/D converters sampling at 18.75 MHz. The hardware digital signal processor (DSP) allows for averaging of complex amplitudes $(I + jQ)$ and/or averaging of power $(I^2 + Q^2)$ before storing on a computer hard disk. Coherent averaging by the DSP hardware reduces the data rate to disk. For example, when 9200 pulses are transmitted in 1 s with 64 coherent averages, the data rate is about 3.6×10^6 bits/s for two channels (I and Q), a 12-bit system, and 1024 samples per pulse $(9200/64*12*2*1024 \approx 3.6 \times 10^6 \text{ bits/s})$. During postprocessing for focused SAR, we apply phase corrections to the stored complex amplitudes of the signal.

C. Scanning Laser Altimeter and GPS Data

The ice-sounding radar data are collected in conjunction with GPS-derived location information and scanning laser altimeter measurements capable of measuring the ice surface topography [20]. As the aircraft moves along the track, the laser altimeter scans the cross-track direction over a swath width centered about the nadir point at the ice surface of about half the aircraft altitude. Thus, for an altitude of 500 m, the scanned cross-track width at the ice surface is about 250 m [21]. The range data from the scanning laser altimeter is processed to extract the ice-surface vector slope (along-track direction and cross-track direction). The nonradar instruments provide ice surface-slope data and the aircraft positional data, which are used to make correction for nonlevel aircraft flight and nonzero surface slopes.
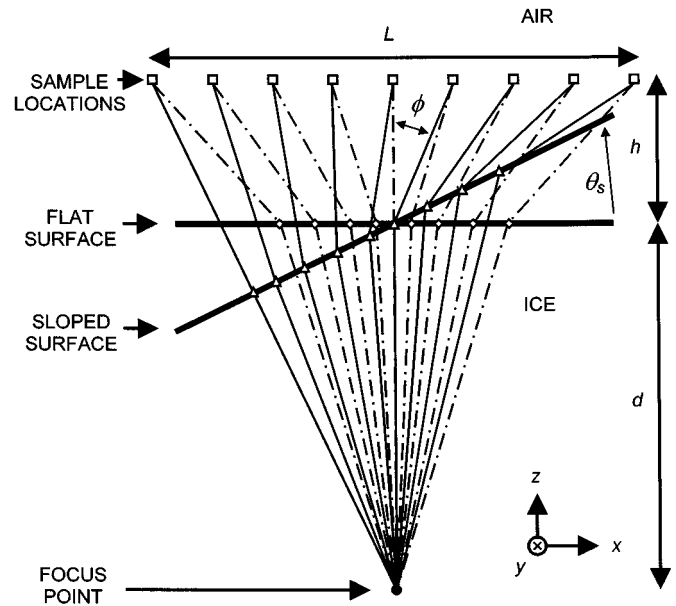

Fig. 1. Illustration of the geometry for focused-SAR processing. Dashed-dot line paths from the ice-sounding-radar sample locations (denoted as squares) in air to the focus point in ice correspond to the flat-ice-surface geometry. Solid line paths from the ice-sounding-radar sample locations in air to the focus point in ice correspond to the sloped-ice-surface geometry. The coordinate system is shown on the figure (the positive y-direction is into the figure).

III. FOCUSED-SAR PROCESSING OF ICE-SOUNDER DATA

A. Measurements Above a Flat Ice Surface

We start by considering the path (obeying Snell's Law) the radar signal takes from a sample location above a flat ice surface (slope angle θ_s equal to zero) to a particular focus point within the ice (we approximated the real part of ice dielectric ε'_{ice} as a constant [7]). Fig. 1 illustrates the imaging geometry. We define $z = 0$ at the air–ice interface of the flat ice surface. We define $x = 0$ at the focus point. For a given sample location ($x = x$, $z = h$) at height h above the ice surface, the range to the focus point at depth d ($x = 0$, $z = -d$) is the sum of the distance in air and ice given by

$$r(x,t) = r_{air}(x,t) + r_{ice}(x,t) \quad (1)$$

where t is the arrival time of the signal return.

The received signal after pulse compression [6] for the sample location is given by

$$a(x,t) = a_0(x,t)e^{j\phi(x,t)} = a_0(x,t)e^{j(\omega_c t - 2kr(x,t))} \quad (2)$$

where
k wavenumber;
ω_c center angular frequency;
a_o real number.

The angular frequency may be rewritten as

$$\omega(x,t) = \frac{d\phi(x,t)}{dt} = \omega_c - 2k\frac{dr(x,t)}{dt} \quad (3)$$

or in terms of frequency

$$f(x,t) = f_c - \frac{2}{\lambda}\frac{dr(x,t)}{dt} \equiv f_c + f_D(x,t). \quad (4)$$

Substituting (1) into (4), we solve for the Doppler frequency, which is given as

$$f_{\mathrm{D}}(x,t) = -\frac{2}{\lambda}\frac{\mathrm{d}r_p}{\mathrm{d}t} = -\frac{2}{\lambda_{\mathrm{air}}}\left[\frac{\mathrm{d}r_{\mathrm{air}}(x,t)}{\mathrm{d}t} + \eta_{\mathrm{ice}}\frac{\mathrm{d}r_{\mathrm{ice}}(x,t)}{\mathrm{d}t}\right] \tag{5}$$

where

λ wavelength;
λ_{air} free-space wavelength;
η_{ice} ice index of refraction.

After downconverting and low-pass filtering (2), we have the signal

$$v(x,t) = a_o'(x,t)e^{-j\theta(x,t)} \tag{6}$$

where

$$\theta(x,t) = 2kr(x,t) = \frac{4\pi}{\lambda_{\mathrm{air}}}\left[r_{\mathrm{air}}(x,t) + \eta_{\mathrm{ice}}r_{\mathrm{ice}}(x,t)\right]. \tag{7}$$

The appropriate reference function for a point target [5] is given by

$$m(x,t) = b(x,t)_{\mathrm{flat}}e^{-j\theta(x,t)} \tag{8}$$

where $b(x,t)_{\mathrm{flat}}$ is a complex correction factor that may include compensation for the received amplitude $a_o'(x,t)$ (such as but not limited to antenna gain, spreading loss, ice surface reflection, media losses, transmitted waveform shape [5]–[7]), and system performance variation. Using the reference function for a point target, correlation between the reference function and the received signal is maximized for a target located at a point. By examining (8) and (9), one notices that the reference function does indeed change for each time (or range). For our study, we simplify the correction factor for a flat surface by setting $b(x,t)_{\mathrm{flat}} = 1$. As presented later in the text, the complex correction factor may be modified to compensate for aircraft motion, $b(x,t)_z$ and also compensate for a nonzero sloped ice surface, $b(x,t)_{\mathrm{slope},z}$.

We focus the data by correlating the signal with the reference function, which is given by

$$\Re_{vm}(x,t) = \int_T\int_L v(x+x',t+\tau)m^*(x',\tau)\,\mathrm{d}x'\mathrm{d}\tau \tag{9}$$

where L is the synthetic-aperture length and the period T (maximum arrival time–minimum arrival time) is the measure of arrival times for a point target for the given synthetic-aperture length, as shown in Fig. 2. The focus point ($x = 0, z = -d$) has samples located along the aperture ($-L/2 < x < L/2, z = h$). Implementation of (9) can be accomplished using range migration by Fourier transform (FT) [22].

When the period T is less than the data sample rate ($T < t_{\mathrm{sample}}$), (9) can be approximated as the following:

$$\Re_{vm}(x,d) = \int_L v(x+x',d)m^*(x',d)\,\mathrm{d}x' \tag{10}$$

where $t_{\mathrm{sample}} = 1/f_{\mathrm{sample}}$ is the data sample time interval and f_{sample} is the data sampling frequency. For the radar described in Section II, f_{sample} is the A/D converter sampling frequency of 18.75 MHz. For $T < t_{\mathrm{sample}}$, the two-dimensional (2-D)
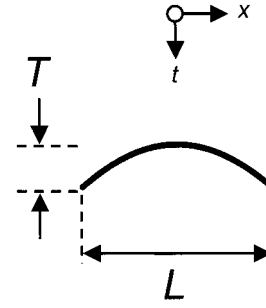

Fig. 2. Point-target time response for the samples corresponding to the synthetic-aperture length L.

functions $v(x,t)$ and $m(x,t)$ for each time are approximated by one-dimensional (1-D) functions $v(x,d)$ and $m(x,d)$ for each depth. Therefore, the correlation is approximately 1-D in x as given by (10) where t and d are related by radar parameters and geometry $t = [2(h + \eta_{\mathrm{ice}}d)]/(\lambda f_c)$.

We implemented (10) using frequency-domain techniques as

$$\Re_{vm}(x,d) = \Im^{-1}\left\{V(f)M^*(f)\right\} \tag{11}$$

where $V(f)$ is the FT of $v(x,d)$ with respect to x and $M(f)$ is the FT of $m(x,d)$ with respect to x.

B. Platform Motion

For focused-SAR processing, we wish the radar platform would travel at a constant velocity, at a constant altitude and in a straight line. Unfortunately, airborne and spaceborne platforms rarely (almost never) behave in such an ideal manner. Without compensation, nonideal platform motion induces phase errors, which degrade the focusing of a SAR processor. Motion compensation techniques are readily available for airborne and spaceborne side-looking radar systems [5].

We investigated nonideal aircraft motion for focused-SAR processing of glacial-ice depth-sounding data. We considered 1-m deviations from the desired ideal travel in the x (along-track speed changes), y (cross-track motion), and z (altitude variation) directions over the synthetic-aperture length for a mean altitude of 500 m and mean velocity in the x-direction of 130 m/s. At the ice surface ($x = 0, z = 0$), the phase error due to a 1-m x-direction deviation Δx is about 0.4° $\{4\pi/\lambda_{\mathrm{air}}[r_{\mathrm{air}}(x + \Delta x) - r_{\mathrm{air}}(x)] \cong 4\pi/2[500.001 - 500]\}$. For a cross-track antenna beamwidth θ_y of about 18°, the cross-track footprint L_y is about 160 m $\{2h\tan(\theta_y/2)\}$. Moreover, for a 1-m y-direction deviation, Δy, the area illuminated changes by less than 2% $\{\sim 2*\Delta y/L_y^**100\% = [1 + 1]/160*100\}$ at the ice surface ($x = 0, z = 0$). At the ice surface ($x = 0, z = 0$), the phase error due to a 1-m z-direction deviation Δz is about 360° $4*\pi/\lambda_{\mathrm{air}}[r_{\mathrm{air}}(z+\Delta z) - r_{\mathrm{air}}(z)] \cong 4\pi/2[501-500]\}$. Platform pitch, roll, and yaw motion for a nadir-looking ice sounder illuminate a given area on the ice surface using an antenna pattern that is shifted accordingly [5]. Based on this analysis, vertical motion contributes the largest phase error for our ice-sounding data.

For the GPS-controlled navigation of the NASA P-3 aircraft, we found that for our typical altitude of 500 m and airspeed of 130 m/s that aircraft motion is not significant (typical deviations

$\ll 1$ m) for apertures on the order of the maximum unfocused aperture length (typically < 50 m). For long synthetic apertures (typically > 100 m), aircraft motion should be compensated.

We compensate for vertical aircraft motion using differential GPS trajectory data. Krabill *et al.* [18] reported that the uncertainty in the laser-derived ellipsoidal height measurements is about 10 cm. Using ellipsoidal height measurements determined from the scanning-laser-altimeter data, we computed the change in an elevation about some mean height

$$\Delta z(x) = h_{\text{elh}}(x) - \bar{h}_{\text{elh}} \tag{12}$$

where

h_{elh} ellipsoidal height;
$\bar{h}_{\text{elh}}$ mean ellipsoidal height;
x along-track position.

We then compute the correction phase associated with this range change from the change in elevation as

$$\psi_{mc}(x) = \frac{4\pi}{\lambda_{\text{air}}} \Delta z(x). \tag{13}$$

Each column (range dimension) is multiplied by the appropriate complex correction factor given by

$$\chi_{mc}(x) = e^{j\psi_{mc}(x)}. \tag{14}$$

Using (14), we applied a phase correction to each pixel, but the location of the return from the same range cell still may be at a different row location (since the timing is from the actual altitude) in the image for each column. Therefore, we shift the pixels of each column accordingly in the image to account for this offset.

Taking into account vertical motion, we write the reference-function complex correction factor as

$$b(x,t)_z = b(x,t)_{\text{flat}} e^{j\psi_{mc}(x)}. \tag{15}$$

C. Slope Ice Surface

Glacial ice often has small surface slopes ($< 2°$). However, for nadir-looking SAR, these small surface slopes can defocus a processor designed for a flat surface. Correcting for the surface slope requires some knowledge of the ice surface topography. A scanning laser altimeter can provide the necessary ice surface topography (vector surface slope). The along-track slope is the most critical since the across-track slope will primarily provide image distortion, not defocusing [5].

Non-zero surface slopes shift the signal phase. If the glacial ice-surface slope has a relatively small change ($< 0.05°$) during the time required to build a synthetic aperture, we can approximate the ice-surface slope as constant for the given aperture. Under this condition, we compute the phase shifts from the following linear model (assumes $\sin\theta_s \approx \theta_s$) for a given ice depth and surface slope angle when $T < t_{\text{sample}}$ as follows:

$$u(x) = ax + p \tag{16}$$

where

u phase shift in degrees;
x along-track position in m;

a model's slope constant;
p model's y-intercept constant.

For ice depths ($d < 4000$ m) and surface slope angles typically found for glacial ice ($-2° < \theta_s < +2°$), we write the phase shifts (16) by expanding a and p. A derivation of the slope correction model is given in Appendix A. The generalized model is written as

$$u_s(x, d, \theta_s) = \left\{ \frac{\theta_s}{\theta_1} a(d)_{\theta_1} \right\} x + \frac{\theta_s^2}{\theta_1^2} \frac{t_1}{s_1} a(d)_{\theta_1} \tag{17}$$

where

u_s phase shift in degrees;
x along-track position in m;
d ice depth in m;
θ_s surface slope angle in degrees;
θ_1 basis surface slope angle in degrees;
$a(d)_{\theta_1}$ slope of the slope-induced phase error as a function of d for θ_1;
t_1 mean y-intercept of the slope-induced phase error over d;
s_1 mean slope of the slope-induced phase error over d.

We corrected the surface slope-induced phase shifts by multiplying the reference function by the following correction function

$$\zeta(x, d, \theta_s) = e^{-ju_s}. \tag{18}$$

Taking into account ice-surface slope and vertical motion, we write the reference-function complex correction factor as follows:

$$b(x, d)_{\text{slope},z} = b(x, d)_z e^{-ju_s}. \tag{19}$$

IV. PROCESSING RESULTS OF A GREENLAND ICE-BEDROCK INTERFACE

We analyzed radar data from an ice-bedrock interface collected in Greenland on June 27, 1998 [23]. For a 132.94-m aperture length, each case was processed using three different methods: 1) incoherent averaging; 2) unfocused-SAR processing; and 3) focused-SAR processing. For each method, we calculated the along-track range resolution and the signal processing gain for a point target. Parameters relating to the data set are given as follows. The real along-track antenna beamwidth θ_a is $72°$, the number of preprocessed coherent integrations (COH) is 64, the pulse repetition frequency (PRF) is 9200 Hz, the real part of the dielectric constant $\varepsilon'_{\text{ice}}$ is 3.17, the aircraft velocity u is about 130 m/s, and the altitude h is about 500 m.

We computed the signal processing gain with an aperture length of 132.94 m for each processing method based on a point-target analysis as shown in Table II. To simplify our analysis of signal processing gain, the signal amplitude factor $a'_o(x, t)$ and the correction factor $b(x, t)$ are assigned a constant value of one. For each method, we determined the number of samples N from the aperture length, repetition frequency, and aircraft velocity ($N = L^* f_p / u$). The repetition frequency f_p is calculated from the PRF and the COH($f_p = \text{PRF}/\text{COH} = 143.75$ Hz). The unfocused-SAR aperture length for a signal phase error less

TABLE II
PROCESSING GAIN IMPROVEMENT FOR A POINT TARGET USING INCOHERENT, UNFOCUSED-SAR AND FOCUSED-SAR PROCESSING, AS DESCRIBED IN THE TEXT

Description	Incoherent Averaging	Unfocused SAR	Focused SAR
Aperture Length, L [m]	132.94	31.65	132.94
Repetition Frequency, f_p [Hz]	143.75	143.75	143.75
Velocity, u [m sec^{-1}]	130	130	130
Samples, $N=L*f_p/u$	147	35	147
Gain Expression	$10\log_{10}N^{0.5}$	$10\log_{10}N$	$10\log_{10}N$
Gain [dB]	10.8	15.4	21.6
Improvement [dB]	-4.6	0.0	+6.2

TABLE III
ALONG-TRACK RANGE RESOLUTION FOR DIFFERENT APERTURE LENGTHS USING INCOHERENT UNFOCUSED-SAR AND FOCUSED-SAR PROCESSING AS DESCRIBED IN THE TEXT

Aperture Length L	Along-Track Resolution [m] $r_a = (h + d / \eta_{ice}) * \lambda_{air} / 2 / L$		
	Incoherent Averaging ($L < 0.90$)	Unfocused SAR ($L < 31.65$)	Focused SAR (L)
0.90 m	1180	1180	1180
31.65 m	1180	34	34
132.94 m	1180	34	8

TABLE IV
RESOLUTION IMPROVEMENT USING INCOHERENT, UNFOCUSED-SAR AND FOCUSED-SAR PROCESSING AS DESCRIBED IN THE TEXT

Aperture Length L	Resolution Improvement $(r_a / r_{a,unfocused\,SAR})$		
	Incoherent Averaging ($L < 0.90$)	Unfocused SAR ($L < 31.65$)	Focused SAR (L)
132.94 m	0.03	1.000	4.250

than $45°$ [5], $\{(h+d/\eta_{ice})\lambda_{air}/2\}^{0.5}$ is based on an altitude h of 500 m and an ice depth d of 1000 m. We used 35 sample points (~ 31.65 m) to approximate the corresponding unfocused-SAR aperture length. Because of signal phase errors ($> 45°$) beyond the unfocused aperture length, the unfocused aperture length is used in the calculation instead of an aperture length of 132.94 m. Under these conditions, the focused-SAR processing-gain improvement is 6.2 dB higher than the unfocused-SAR improvement.

We computed the along-track range resolution with an aperture length of 132.94 m for each processing method, as shown in Tables III and IV. To simplify our analysis of along-track range resolution, the signal amplitude factor $a_o'(x, t)$ and the correction factor $b(x, t)$ are assigned a constant value of 1. We calculated the along-track range resolution r_a, ($[h+d/\eta_{ice}]*\lambda_{air}/2/L$) using the aperture lengths as explained in the following text. Incoherent averaging does not improve the along-track range resolution. Hence, the raw data aperture length of about 0.9 m is used for computation. For phase errors less than about $45°$ (~ 31.65 m), unfocused-SAR processing improves the along-track range resolution. However, for larger apertures, the signal experiences coherent degradation due to large phase errors ($> 45°$). Thus, unfocused-SAR aperture length is limited to about 31.65 m for the resolution calculation. As discussed in Section III for focused SAR, the signal is phase-corrected using $\theta(x, t)$. Therefore, an aperture length of 132.94 m is used for resolution computation. Under these conditions, the focused-SAR along-track resolution improvement is 4.25 times better than unfocused-SAR improvement.

We compensated the radar data for vertical aircraft motion and first-order compensated for the sloped ice surface. We applied phase corrections (8) with $b(x, d)_{slope, z}$ to the radar data for a surface slope of $0.4°$, which represents a mean slope value over the image. The ice-surface slope data are obtained from the scanning laser altimeter data as described in Section II. Fig. 3 shows the raw radar image and the processed results for an aperture length of 132.94 m (147 sample points).

First, we make a few initial observations regarding the images of the ice–bedrock interface produced from the radar ice-sounding data as shown in Fig. 3. For a cross-track antenna beamwidth in air θ_y of about $18°$, the cross-track
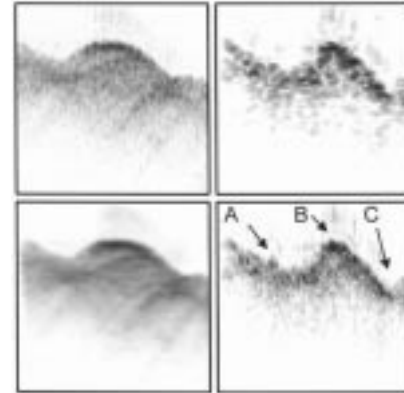

Fig. 3. Processed data collected in Greenland from an ice–bedrock interface. The top of each frame corresponds to a depth of 930 m, whereas the bottom of the frame is 360 m deeper at a depth of 1290 m. The horizontal axis starts on the left at 0-m distance and proceeds to the right to 1800-m distance for each frame. Top left frame corresponds to raw data (no postprocessing). Bottom left frame corresponds to incoherently processed data. Top right frame corresponds to unfocused-SAR processed data. Bottom right frame corresponds to focused-SAR processed data. The focused-SAR image shows a small hill (designated by A), a large hill (designated by B), and a valley (designated by C), which were extracted from the raw signal clutter.

footprint at a depth of 1000 m is about 335 m $(2h \tan[\theta_y/2] + 2d \tan[\theta_y/\eta_{ice}/2])$. We did not employ any method to reduce clutter from the cross-track footprint. Thus, below the ice-interface boundary, clutter due to the cross-track beamwidth is present. Above the ice-interface boundary, we see a weaker duplicate signal (so-called ghost), which is due to radar range sidelobes [24] (peak sidelobe is about 30-dB down from peak).
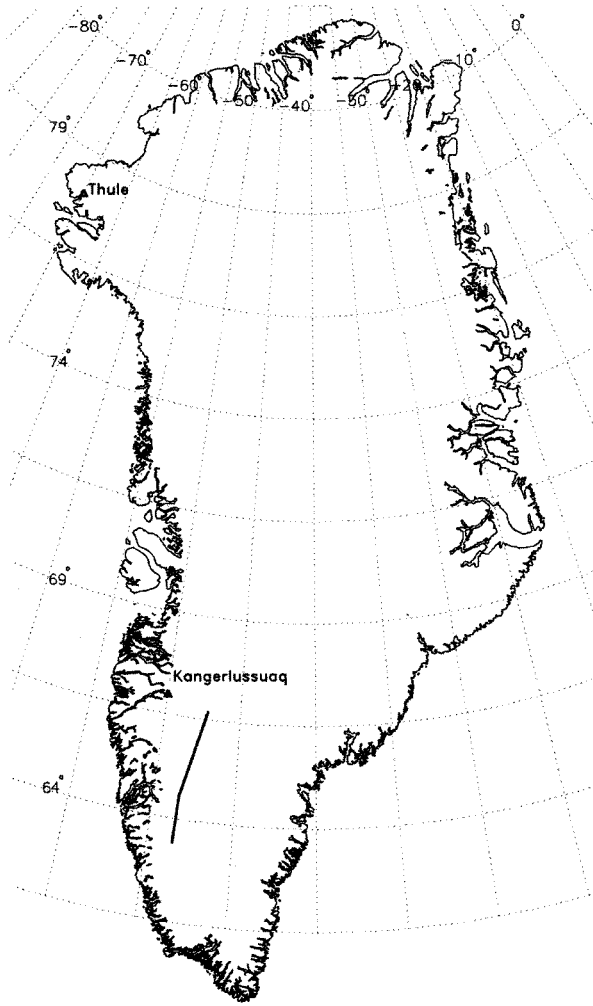
Fig. 4. Map illustrates the portion of the 2000-m contour line of southwest Greenland where quality ice-thickness measurements were missing.
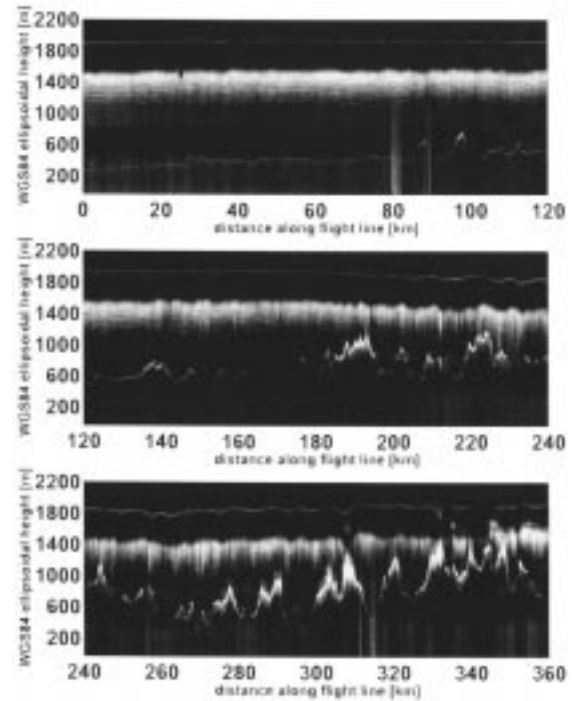

Fig. 5. Focused images from the 360-km southwest-Greenland 2000-m contour line, which was flown in 1998, where high-quality ice thickness data have been sparse. We use the WGS84 ellipsoidal height for the y-axis label and distance along the flight line for the x-axis label. The top of the ice sheet is at elevations from about 1800 m to 2000 m. About the first 300 m shown below the top are a dark color due to receiver blanking. The ice-bedrock interface starts at an elevation of about 250 m and ranges from about 250-m to 1400-m elevations.

The incoherent processing results from Fig. 3 illustrate that along-track resolution remains the same after integration, which agrees with our computation ($r_a = 1180$ m from Table III). However, the incoherent integration low-pass filters the data; hence, the smoothed appearance for the longer aperture.

The unfocused-SAR processing results from Fig. 3 show coherent degradation (due to the phase errors of greater than $45°$ for the 132.94-m aperture) of the radar signal for an aperture consisting of 147 sample points. The along-track resolution ($r_a = 34$ m from Table III) improves with longer apertures up to the maximum unfocused-aperture length (~ 31.65 m). Thus, after reaching the maximum unfocused-aperture length, additional integrations coherently degrade the radar image.

The focused-SAR results from Fig. 3 show that along-track resolution improves with longer apertures (147 sample points corresponds to $r_a \approx 8$ m from Table III). The focused-SAR processing results and unfocused-SAR processing results are approximately identical, as Table III illustrates, up to the maximum unfocused aperture length (~ 31.65 m). After reaching the maximum unfocused aperture length, the resolution is improved only in the focused case and coherent degradation occurs for the unfocused-SAR case for an aperture of 132.94 m.

Comparing the focused-SAR image to the raw data image from Fig. 3, we see that several features are extracted from the clutter at the ice-bedrock interface. We notice the small hill around 0.5 km (designated on Fig. 3 as point A), which is extracted from the signal clutter present in the raw data. The focused-SAR results with an aperture length of 132.94 m have more definition of the peak around 1.0 km (designated on Fig. 3 as point B). Also, the valley around 1.5 km (designated on Fig. 3 as point C) is extracted from the signal clutter present in the raw data.

V. ICE THICKNESS FROM SOUTHWEST GREENLAND 2000-m CONTOUR LINE

A lack of ice-thickness measurements over southwest Greenland 2000-m contour line led to the July 18, 1998 ice-sounding flight, where coherent radar data were collected over southwest Greenland [23]. These data were collected under heavy melt conditions where ponds and streams were observed on the ice surface. These ice thickness measurements were needed for improving mass-balance estimates of the Greenland ice sheet. In this section, we present the focused-SAR image and the ice thickness data extracted from the radar data.

Using focused-SAR processing, we processed data collected over a key 360-km-long portion of the 2000-m contour line of southwest Greenland. Fig. 4 illustrates this key portion of the southwest-Greenland flight line, which is superimposed on a
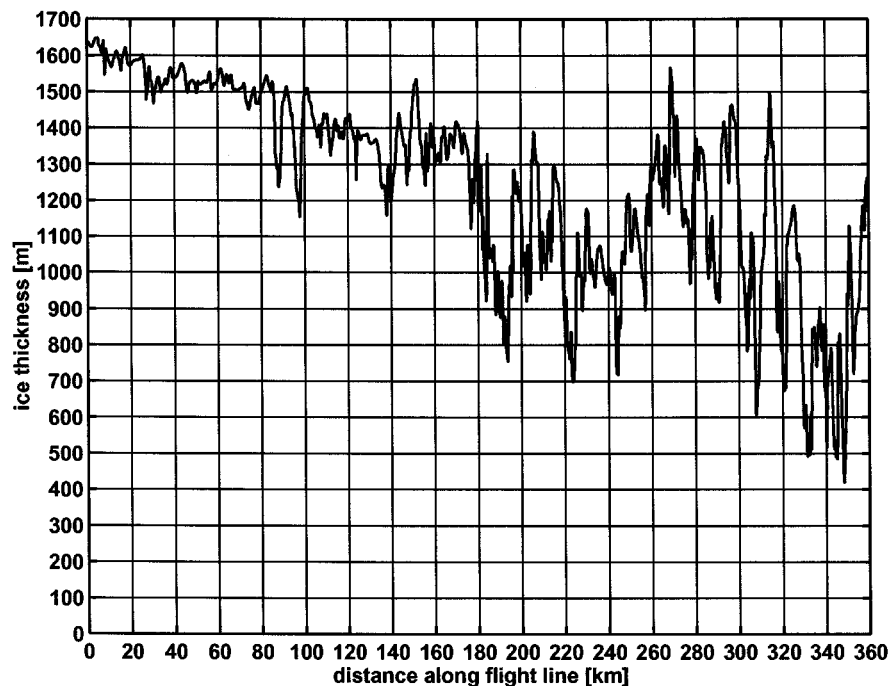
Fig. 6. Ice thickness data measured along the 360-km southwest-Greenland 2000-m contour line flown on July 18, 1998. Data were collected under heavy melt conditions.

map of Greenland. Parameters relating to the data set are given as follows.

Real along-track antenna beamwidth θ_a	72°;
Number of preprocessed COH	128;
PRF	15 000 Hz;
Real part of the dielectric constant $\varepsilon'_{\text{ice}}$	3.17;
Aircraft velocity u	130 m/s^{-1};
Altitude h	150 m;
Repetition frequency f_p	117.19 Hz.

Using point-target analysis as described in Section IV for an ice depth of 1650 m, focused-SAR processing ($N = 165$ samples, $L = 180$ m, $r_a = 6$ m) has a 7.5-dB processing gain advantage and a 5.6-times finer along-track resolution advantage over unfocused-SAR processing ($N = 29$ samples, $L = 31.9$ m and $r_a = 33.8$ m). As described in Section III, we compensated the radar data for vertical aircraft motion and first-order compensated for the sloped ice surface where the ice-surface slope slowly varies (dividing the ice-surface slope data from the first 180-km line into 180-m apertures, we find the majority of apertures have slope changes less than 0.05°) across about the first 180 km of the flight line with a mean slope of about −0.05° (∼ flat surface). However, for the second 180 km of the flight line, the ice-surface slope is rapidly varying (dividing the ice-surface slope data from the second 180-km line into 180-m apertures, we find that 75% of these aperture have slope changes from 0.05° to 0.35°), which means the approximation of constant slope over the 180-m aperture is poor. Because the condition of slow-varying ice-surface slope during an aperture is not satisfied, the first-order slope compensation is not applied for the second portion of the line.

The focused-SAR image over the key portion of the 2000-m contour line in southwest Greenland is shown in Fig. 5.

The ice surface (air-ice interface) is located at ellipsoidal heights between about 1800 m to 2000 m. The bottom surface (ice-bedrock interface) is located at ellipsoidal heights between about 250 m and 1400 m. The first, about 300 m below the ice surface, is a dark color (weak signal) because the radar uses a signal blanking circuit to avoid receiver saturation from returns near the ice surface. Well known internal ice layering [7] is seen in the focused-SAR image at ellipsoidal heights between about 1500 m to near the bottom surface. For the first 180-km portion of the flight line, the ice internal layering is imaged continuously. For the second 180-km portion of the flight line, the ice internal layering in the image is occasionally blurred, which we believe is at least in part due to the rapidly varying ice-surface slope. Bottom topography becomes increasingly rough toward the southern end of the flight line with peak-to-peak deviations of about 1100 m. The ice thickness decreased from about 1700 m at the start of the flight (66.65°N, 47.22°W) to about 400 m at the end of the flight (63.52°N, 48.49°W) as shown in Fig. 6.

The ice thickness measurements reported here along the southwest Greenland 2000-m contour line filled the ice-thickness data gap for the 2000-m contour line of all Greenland. We believe that we obtained reliable ice-thickness data for this key area through the combination of the advanced ice-sounding radar system with SAR processing. These new data allowed for a better understanding of the of mass-balance at high elevations to be achieved [25].

VI. CONCLUSION

The synthesis of the modern ice-sounding radar system with SAR processing allowed us to obtain ice-thickness measurements over a key portion of the southwest Greenland 2000-m

contour line, which were needed for a better mass-balance estimate of the Greenland ice sheet.

By an analysis of an ice-bedrock interface, we demonstrated that coherent ice-sounding radar data can be focused in the along-track direction using SAR processing, which sharpens image resolution. The improved along-track resolution defined bedrock topography more accurately than by using unfocused-SAR processing or incoherent averaging. The focused-SAR processing improved along-track resolution by a factor of about four and provided about 6-dB processing gain over that for unfocused-SAR processing based on a point-target analysis.

The focused-SAR processing presented here has additional potential uses for ice-sounding systems. The demonstrated processor can be applied to data collected from nadir-looking spaceborne ISR systems. Also, we expect thin ice, such as that found along the ice sheet margins, will be imaged better as in Section IV, because along-track surface-return clutter will be reduced using SAR focusing. However, we must remind one that the cross-track surface clutter is not reduced using focused-SAR processing. The cross-track surface clutter may be reduced by narrowing the cross-track beamwidth of a nadir-looking ice-sounding radar.

APPENDIX
CORRECTION MODEL DERIVATION FOR A SLOPED ICE SURFACE

We derive a linear-based $(\sin\theta_s \approx \theta_s)$ correction model for a sloped ice surface. We approximated the real part of the ice dielectric, $\varepsilon'_{\text{ice}}$, as constant [7] for glacial ice. The authors make no attempt to correct for nonconstant values $(\varepsilon'_{\text{ice}})$ that occur in the firn layer above the glacial ice. We compute the phase shifts with units of degrees as a function of sample location, x, focus-point depth d and the ice surface slope angle θ_s as

$$u_s(x,d,\theta_s) = a(d,\theta_s)x + p(d,\theta_s) \tag{A.1}$$

where a is the model's slope constant and p is the model's y-intercept constant.

For a zero-phase shift for a given slope angle, we have

$$u_s(x,d,\theta_s) = 0 \tag{A.2}$$

or

$$p(d,\theta_s) = -a(d,\theta_s)x. \tag{A.3}$$

Using the geometry from Fig. 1, we write

$$\sin\phi = \frac{x}{h} \tag{A.4}$$

or

$$x = h\sin\phi \tag{A.5}$$

which for small angles is approximately

$$x = h\phi \tag{A.6}$$

where the zero-phase shift angle, ϕ is the angle made between the vertical line $(x = 0)$, and the sample location where the zero-phase shift occurs for the ice-surface slope angle. The

angle ϕ is proportional to the slope angle θ_s, which can be rewritten as

$$x = v_{\text{constant}}\theta_s \tag{A.7}$$

where the constant v_{constant} is approximately constant for the conditions described in Section III. Now we rewrite

$$p(d,\theta_s) = -v_{\text{constant}}\theta_s\, a(d,\theta_s). \tag{A.8}$$

For a given slope angle $\theta_s = \theta_1$, we write (A.8) as

$$p(d)_{\theta_1} = -v_{\text{constant}}\theta_1 a(d)_{\theta_1} \tag{A.9}$$

where a and p are computed from the imaging geometry for the basis slope angle $\theta_s(\theta_s \neq 0)$. Integrating both sides over depth and normalizing (A.9), we write

$$\frac{\int_d p(d)_{\theta_1}\mathrm{d}d}{\int_d \mathrm{d}d} = -v_{\text{constant}}\theta_1 \frac{\int_d a(d)_{\theta_1}\mathrm{d}d}{\int_d \mathrm{d}d}. \tag{A.10}$$

From (A.10), we define two model parameters

$$t_1 = \frac{\int_d p(d)_{\theta_1}\mathrm{d}d}{\int_d \mathrm{d}d} \tag{A.11}$$

and

$$s_1 = \frac{\int_d a(d)_{\theta_1}\mathrm{d}d}{\int_d \mathrm{d}d}. \tag{A.12}$$

Now we solve (A.10) using (A.11) and (A.12) for the constant, v_{constant} as

$$v_{\text{constant}} = -\frac{t_1}{s_1\theta_1}. \tag{A.13}$$

Using the result (A.13), we rewrite the (A.8) for the model's y-intercept constant as

$$p(d,\theta_s) = \frac{\theta_s}{\theta_1}\frac{t_1}{s_1}a(d,\theta_s). \tag{A.14}$$

From the linear assumption, the model's slope constant is given by

$$a(d,\theta_s) = \frac{\theta_s}{\theta_1}a(d)_{\theta_1}. \tag{A.15}$$

As described in Section III, we write the phase shifts (A.1) by expanding a and p. The generalized model is written as

$$u_s(x,d,\theta_s) = \left\{\frac{\theta_s}{\theta_1}a(d)_{\theta_1}\right\}x + \frac{\theta_s^2}{\theta_1^2}\frac{t_1}{s_1}a(d)_{\theta_1}. \tag{A.16}$$

The model parameters t_1, s_1, a, and p need to be computed only once from the geometry with slope angle of θ_1. The phase shifts for the slope angle θ_s are determined from the model using the values for t, s, a and p for θ_1 from a look-up table.

data-collection missions from Goddard Space Flight Center's Wallops Flight Facility, Wallops Island, VA, especially Dr. W. Krabill, Dr. C. Martin, Dr. W. Abdalati, Mr. D. Young, and the pilots and flight crew who safely returned us from our Greenland adventures.

REFERENCES

[1] J. J. Legarsky, S. P. Gogineni, P. Kanagaratnam, T. L. Akins, and Y. C. Wong, "Ice thickness measurements of the southwest Greenland 2000-m contour line," in *Proc. Int. Geoscience and Remote Sensing Symp.*, Hamburg, Germany, June–July 28–2, 1999, pp. 89–91.

[2] D. J. Daniels, *Surface-Penetrating Radar*. London, U.K.: IEE, 1996.

[3] J. I. Halman, K. A. Shubert, and G. T. Ruck, "SAR processing of ground-penetrating radar data for buried UXO detection: Results from a surface-based system," *IEEE Trans. Antennas Propagat.*, vol. 46, pp. 1023–1027, July 1998.

[4] J. P. Porcello, R. L. Jordan, J. S. Zelenka, G. G. Adams, R. J. Phillips, W. E. Brown Jr, S. H. Ward, and P. L. Jackson, "The Apollo lunar sounder radar system," *Proc. IEEE*, vol. 62, pp. 769–783, June 1974.

[5] F. T. Ulaby, R. K. Moore, and A. K. Fung, *Microwave Remote Sensing*. Norwood, MA: Artech House, 1982, vol. 2.

[6] G. Franceschetti and R. Lanari, *Synthetic Aperture Radar Processing*. Boca Raton, FL: CRC, 1999.

[7] V. V. Bogorodsky, C. R. Bentley, and P. E. Gudmandsen, *Radioglaciology*. Dordrecht, The Netherlands: Reidel, 1985.

[8] C. R. Bentley, N. Lord, and C. Liu, "Radar reflections reveal a wet bed beneath stagnant ice stream C and a frozen bed beneath ridge BC, west Antarctica," *J. Glaciol.*, vol. 44, no. 146, pp. 149–156, 1998.

[9] B. C. Welch, W. T. Pfeffer, J. T. Harper, and N. F. Humphrey, "Mapping subglacial surfaces of temperate valley glaciers by two-pass migration of a radio-echo sounding survey," *J. Glaciol.*, vol. 44, no. 146, pp. 164–170, 1998.

[10] N. A. Nereson, C. F. Raymond, E. D. Waddington, and R. W. Jacobel, "Migration of the siple dome ice divide, west Antarctica," *J. Glaciol.*, vol. 44, no. 148, pp. 643–652, 1998.

[11] A. Herique and W. Kofman, "Determination of the ice dielectric permittivity using the data of the test in Antarctica of the ground-penetrating radar for Mars'98 Mission," *IEEE Trans. Geosci. Remote Sensing*, vol. 35, pp. 1338–1349, Sept. 1997.

[12] G. Raju and R. K. Moore, "A matched-filter technique for removing hyperbolic effects due to point scatterers: Simulation and application on Antarctic radar data," *IEEE Trans. Geosci. Remote Sensing*, vol. 28, pp. 726–729, July 1990.

[13] D. Dahl-Jensen, N. S. Gundestrup, S. J. Johnsen, K. Keller, S. P. Gogineni, C. T. Allen, T. S. Chuah, H. Miller, S. Kipfstuhl, and E. D. Waddington, "A search in north Greenland for a new ice-core drill site," *J. Glaciol.*, vol. 43, no. 144, pp. 300–306, 1997.

[14] E. J. Rignot, S. P. Gogineni, W. B. Krabill, and S. Ekholm, "North and Northeast Greenland ice discharge from satellite radar interferometry," *Science*, vol. 276, pp. 934–937, May 1997.

[15] J. Legarsky, A. Wong, T. Akins, and S. P. Gogineni, "Detection of hills from radar data in central-northern Greenland," *J. Glaciol.*, vol. 44, no. 146, pp. 182–184, 1998.

[16] W. Krabill, W. Abdalati, E. Frederick, S. Manizade, C. Martin, J. Sonntag, R. Swift, R. Thomas, W. Wright, and J. Yungel, "Greenland ice sheet: High-elevation balance and peripheral thinning," *Science*, vol. 289, pp. 428–430, July 2000.

[17] R. H. Thomas, W. Abdalati, T. L. Akins, B. M. Csatho, E. B. Frederick, S. P. Gogineni, W. B. Krabill, S. S. Manizade, and E. J. Rignot, "Substantial thinning of a major east Greenland outlet glacier," *Geophys. Res. Lett.*, vol. 27, pp. 1291–1294, May 2000.

[18] S. Gogineni, T. Chuah, C. Allen, K. Jezek, and R. K. Moore, "An improved coherent radar depth sounder," *J. Glaciol.*, vol. 44, no. 148, pp. 659–669, 1998.

[19] M. Skolnik, *Radar Handbook*. New York: McGraw-Hill, 1990.

[20] W. B. Krabill, C. W. Wright, R. N. Swift, E. B. Frederick, S. S. Manizade, J. K. Yungel, C. F. Martin, J. G. Sonntag, M. Duffy, W. Hulslander, and J. C. Brock, "Airborne laser mapping of assateague national seashore beach," *Photogramm. Eng. Remote Sensing*, vol. 66, no. 1, pp. 65–71, 2000.

[21] W. Krabill, R. Thomas, C. Martin, R. Swift, and E. Fredrick, "Accuracy of laser altimetry over the Greenland ice sheet," *Int. J. Remote Sensing*, vol. 16, no. 7, pp. 1211–1222, 1995.

[22] R. H. Stolt, "Migration by Fourier transform," *Geophysics*, vol. 43, no. 1, pp. 23–46, 1978.

[23] S. P. Gogineni, D. Tammana, and K. Shepherd. Remote Sensing of Polar ice. Univ. Kansas, Lawrence. [Online]. Available: http://tornado.rsl.ukans.edu/

[24] D. R. Wehner, *High Resolution Radar*. Norwood, MA: Artech House, 1987.

[25] R. Thomas, T. Akins, B. Csatho, M. Fahnestock, P. Gogineni, C. Kim, and J. Sonntag, "Mass balance of the Greenland ice sheet at high elevations," *Science*, vol. 289, July 2000.

Justin J. Legarsky (S'98–M'99) received the M.S. and Ph.D. degrees in electrical engineering from the University of Kansas, Lawrence, in 1995 and 1999, respectively. He received the B.S. degree in electrical engineering from the University of Washington, Seattle, in 1993.

Currently, he is an Assistant Professor of Electrical Engineering and a Member of the Institute for the Development of Commercial Remote Sensing Technologies (ICREST), University of Missouri, Columbia. His current remote sensing research interests include optical and SAR sensor data fusion, ground penetrating SAR for landmine detection, and radar sounding of the glacial ice sheets. From 1999 to 2000, he was with the Jet Propulsion Laboratory, California Institute of Technology, Pasadena, where he worked in the Radar Science and Engineering Section. He was involved in the development of the Mars Advanced Radar for Subsurface and Ionospheric Sounding (MARSIS). Prior to joining JPL, he was with the Radar Systems and Remote Sensing Laboratory, University of Kansas, from 1994 to 1999.

Dr. Legarsky is a member of the American Geophysical Union.

Sivaprasad P. Gogineni (S'75–M'76–SM'91–F'99) received the Ph.D. degree from the University of Kansas (UK), Lawrence, in 1984.

He is currently the Deane E. Ackers Distinguished Professor of Electrical Engineering and Computer Science, UK. He was a Visiting Assistant Professor and Research Engineer with UK during 1984 and from 1985 to 1986. He joined the Electrical Engineering and Computer Science Department as an Assistant Professor in November 1986. He has been with UK since, except for a sabbatical during the 1992–1993 academic year, when he was at the Byrd Polar Research Center, The Ohio State University, Columbus. Also, in 1997 and 1998, he was on leave from UK to work as Manager of the Polar Research Program, NASA Headquarters, Washington, DC. He is the former director of the Radar Systems and Remote Sensing Laboratory. His research includes extensive work on the application of radars to the remote sensing of sea ice, ocean, atmosphere, and land. He has authored or been a co-author of 60 archival journal publications and more than 110 technical reports and conference presentations. He developed several radar systems currently being used at UK for backscatter measurements and has also participated in field experiments in the Arctic and on towers in the open ocean.

Dr. Gogineni is a member URSI Commission F and the Electromagnetics Academy. In 1991, he was awarded the Miller Award for Engineering Research from the University of Kansas and the Taylor and Francis Best Letter Award. He was the Editor of the Newsletter of the IEEE Geocience and Remote Sensing Society from 1994 to 1997, and also received a best-of-session award from the Third International Airborne Remote Sensing Conference in 1997. He was given the NASA Terra award in 1998. In 1999, he was awarded United States Patent 5 867 117 for a swept-step radar system and its detection method. Also, during 1999 he led the working group on the study of collaboration between NASA and ESA, and NASA and NASDA in Earth Sciences. In 2000, he received the Miller Professional Development Award for distinguished service to the engineering profession from UK. NASA awarded him its Group Achievement Award to the Antarctic Mapping Mission Team.

Torry L. Akins, photograph and biography not available at the time of publication.